Progress In Electromagnetics Research C, Vol. 171, 529–540, 2026 PIER C

(Received 29 May 2026, Accepted 25 June 2026, Scheduled 24 July 2026)

Torque Ripple Suppression Strategy for Switched Reluctance Motors Based on Online Torque Correction and Switching Angle Optimization

Huan Liu, Junxin Xu*, Chaozhi Huang, Zikai Wei, and Zhifeng Liu

School of Electrical Engineering and Automation, Jiangxi University of Science and Technology, Ganzhou, Jiangxi 341000, China

ABSTRACT: To address excessive torque ripple in switched reluctance motors (SRMs) during commutation intervals, this paper proposes an interval-based online torque-correction control strategy that uses a correction factor. First, a first-order discretized predictive model is established to estimate the output torque boundary in real time, thereby defining the dynamic constraint range of the reference torque. Subsequently, the commutation zone is divided into two sub-intervals based on the inductance characteristics, and a dynamic correction factor is introduced to perform online torque correction. This mechanism ensures a smooth torque transition during commutation by adjusting the reference torque. Furthermore, the Particle Swarm Optimization (PSO) algorithm is employed for global offline optimization of the turn-on and turn-off angles under full operating conditions to determine the optimal conduction0angle combination. Simulation analysis and experimental results demonstrate that, compared with traditional methods, the proposed strategy significantly reduces the torque ripple and peak phase current across various operating conditions, effectively enhancing the system's stable operating performance and dynamic tracking accuracy.

1. INTRODUCTION

Switched Reluctance Motors (SRMs) feature a simple structure, low cost, and robust fault-tolerant capability, demonstrating broad application prospects in fields such as electric vehicle drives and aerospace [1, 2]. However, their doubly salient structure and highly saturated magnetic circuits inevitably lead to significant torque ripples during operations. This results in severe vibrations and acoustic noise, thereby restricting their high-performance applications [3–5].

To promote the widespread adoption of SRMs, researchers have proposed various control strategies centered on torque ripple suppression, including current chopping control (CCC) [6], direct instantaneous torque control (DITC) [7], and torque sharing function (TSF) control [8]. Among them, TSF control has emerged as one of the most effective strategies for mitigating SRM torque ripples. However, under different operating conditions, the torque tracking capability of TSF-based control strategies is severely degraded, thereby constraining their applicable operating range [9, 10].

Numerous studies have been conducted to enhance the conventional TSF strategy and improve its performance. A seven-level T-type converter was introduced in [11] to improve the voltage utilization during the commutation intervals. Dual sliding mode control and high-efficiency TSF methods were proposed in [12, 13] to enhance the speed regulation performance and reduce the torque ripple, respectively.

In addition, the selection of the turn-on and turn-off angles is closely related to the TSF. In [14, 15], the excitation current establishment and demagnetization current decay processes during commutation intervals were improved by optimizing the turn-on and turn-off angles, thereby reducing the torque ripple and enhancing the operating efficiency. Similarly, in [16], a modified crow search algorithm was employed to optimize the switching parameters of SRM drives to suppress torque ripples and improve dynamic performance.

Furthermore, various torque compensation and correction strategies based on the TSF framework have been proposed to improve the commutation performance and suppress the torque ripple under TSF control [17–20]. However, the achievable torque limit and the insufficient excitation torque capacity during commutation have not been fully considered. In [21], an optimized torque sharing function dynamically adjusts the reference torque during commutation to improve the tracking of the high-speed torque. However, it uses unified correction rules for the whole commutation interval and ignores physical torque output limits. In [22], the sliding mode control compensates torque ripples from the demagnetization tail current. However, it lacks segmented commutation control and real-time torque constraints, and fixed switching angles degrade performance under varying loads and speeds. In [23], the torque error between reference and instantaneous torque is fed back to the incoming phase for torque correction, ignoring its inadequate output capacity at early commutation.

Nevertheless, existing torque correction methods still suffer from several limitations, including the failure to perform differentiated compensation by partitioning commutation regions, the absence of explicit torque feasibility constraints, and the re-

* Corresponding author: Junxin Xu (xujx9997@163.com).

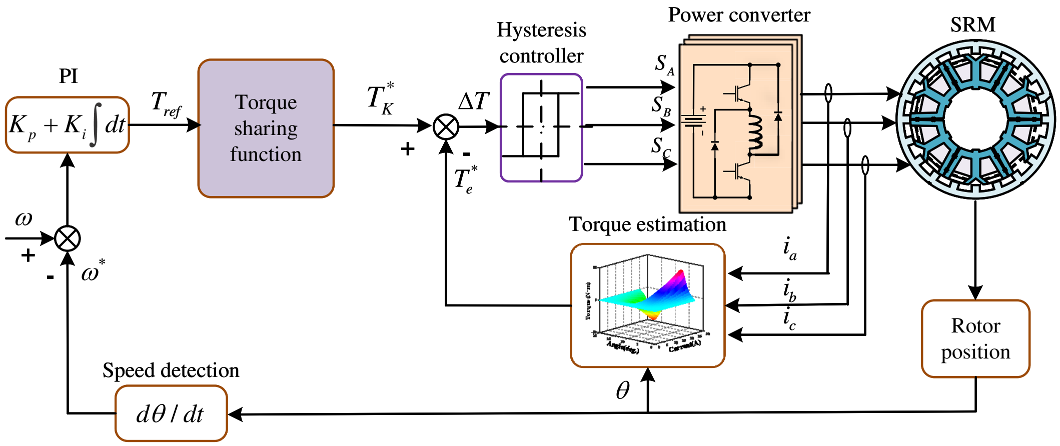

FIGURE 1. Block diagram of the conventional TSF system.

liance on fixed compensation rules and switching parameters. These limitations degrade the torque stability of such methods across various speed and load operating points.

To address these issues, this paper proposes a partition-based online torque correction strategy combined with Particle Swarm Optimization (PSO)-based switching angle optimization to form a coordinated offline-online control framework for SRM torque regulation. Unlike existing methods that adopt a unified compensation mechanism throughout the whole commutation cycle without segmented compensation schemes for TPE1 and TPE2, while ignoring the torque output boundary constraints of the motor during commutation. In contrast, the proposed method implements partition-based online torque correction and introduces position-dependent correction factors to dynamically adjust the reference torque.

The main contributions are summarized as follows: (1) The entire commutation process is divided into two subintervals to realize partitioned online torque correction. (2) A torque prediction model is established to guarantee that all corrected reference torques stay within the actual feasible torque output range of the motor. (3) A position-dependent correction factor is adopted to achieve smooth torque regulation. (4) PSO is employed to optimize switching angles under various operating conditions.

2. CONVENTIONAL TSF CONTROL STRATEGY

For an SRM, the phase voltage equation can be expressed as follows:

$$U_k = R_k i_k + \frac{d\varphi_k}{dt} \tag{1}$$

where U_k, i_k, and R_k denote the phase voltage, phase current, and phase resistance, respectively. φ_k represents the phase flux linkage, which is a nonlinear function of the rotor position θ and phase current i_k.

By expanding the flux linkage derivative, the current variation rate can be obtained as follows:

$$\frac{di_k}{dt} = \frac{U_k - R_k i_k - \omega \frac{\partial \varphi_k}{\partial \theta}}{\frac{\partial \varphi_k}{\partial i_k}} \tag{2}$$

where ω denotes motor speed. As shown in Equation (2), the current variation rate is determined by the motor speed, phase voltage, and phase flux linkage.

To simplify the analysis, the electromagnetic torque of the SRM can be approximately expressed using the linear inductance model as follows:

$$T_k(\theta, i_k) = \frac{1}{2} i_k^2 \frac{\partial L(\theta, i_k)}{\partial \theta} \bigg|_{i_k = \text{const}}, \quad k = 1, 2, 3 \tag{3}$$

where $T_k(\theta, i_k)$ is the electromagnetic torque of the k-th phase, i_k the phase current, θ the rotor position angle, and $L(\theta, i_k)$ the phase inductance.

The TSF control method is widely used for torque ripple suppression in SRMs. The structural diagram of the TSF control system is shown in Fig. 1. First, the total torque reference T_{ref} derived from the speed loop is distributed in individual phase torque references $T_{k\text{ref}}$ via the torque-sharing function. Meanwhile, the actual phase torque T_k is calculated using the measured phase currents and rotor position. Finally, the torque error ΔT is fed into a hysteresis controller to regulate the switching states, thereby enforcing accurate torque tracking and minimizing the overall torque ripple.

Based on the control principle of the TSF, the summation of the individual phase torque sharing functions remains equal to unity at any instant. The general formulation of TSF is defined as follows:

$$\begin{cases} T_k(\theta) = T_{\text{ref}} f_k(\theta), & k = 1, 2, \cdots, m \\ \sum_{k=1}^{m} f_k(\theta) = 1, & 0 \le f_k(\theta) \le 1 \end{cases} \tag{4}$$

where T_{ref} represents the total reference torque, $f_k(\theta)$ the TSF for the k-th phase, and $T_k(\theta)$ the reference torque for the k-th phase. Common TSF types include linear, cubic, exponential, and cosine. The exponential type achieves better torque ripple

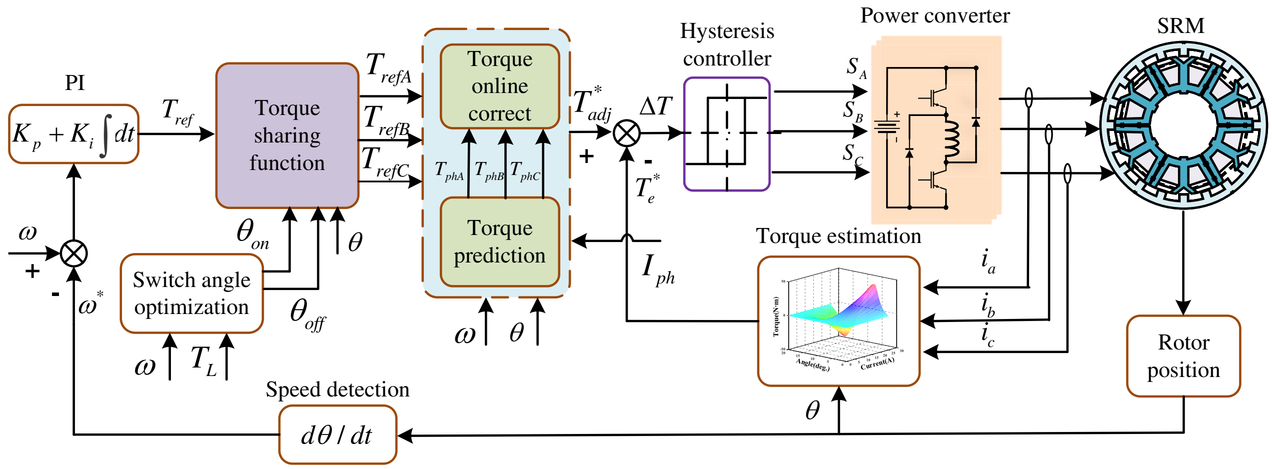

FIGURE 2. Block diagram of the proposed TOC strategy.

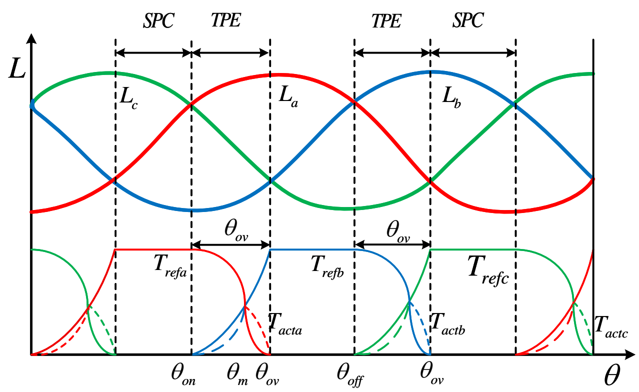

FIGURE 3. Inductance characteristics and TSF profiles.

suppression performance, and the expression is as follows:

$$f_j(\theta) = \begin{cases} 1 - \exp\left(-\dfrac{(\theta - \theta_{\text{on}})^2}{\theta_{\text{ov}}}\right), & \theta_{\text{on}} \le \theta \le \theta_{\text{on}} + \theta_{\text{ov}} \\ 1, & \theta_{\text{on}} + \theta_{\text{ov}} \le \theta \le \theta_{\text{off}} \\ \exp\left(-\dfrac{(\theta - \theta_{\text{off}})^2}{\theta_{\text{ov}}}\right), & \theta_{\text{off}} \le \theta \le \theta_{\text{off}} + \theta_{\text{ov}} \\ 0, & \theta_{\text{off}} + \theta_{\text{ov}} \le \tau_r \end{cases} \quad (5)$$

In the TSF control strategy, a significant torque ripple is typically generated when the machine operates within the commutation region.

(1) In the early stage of commutation, the demagnetization phase approaches the unaligned rotor position, where the inductance variation rate is relatively low. According to Equation (3), the generated torque is proportional to the inductance gradient. Therefore, the excitation phase current cannot be established rapidly enough to produce the desired torque, resulting in an insufficient torque output and a temporary reduction in the total electromagnetic torque.

(2) During the later commutation stage, the excitation phase approaches the aligned rotor position with a relatively high inductance. Owing to the slow decay of the demagnetization phase current, the actual torque cannot decrease rapidly enough to track the reference torque, which leads to excessive torque output and severe tail-current-induced torque ripple.

Furthermore, factors such as an increase in speed and constraints of the bus voltage exacerbate both situations. Fig. 3 illustrates the inductance characteristics and TSF profiles of the SRM, where the solid and dashed lines represent the reference phase torque allocated by the TSF and the instantaneous actual phase torque, respectively.

3. TORQUE ONLINE CORRECTION CONTROL STRATEGY

3.1. Torque Prediction and Commutation Region Division

As further revealed by the torque characteristic analysis of SRMs, apart from the aforementioned drawbacks of uniform fixed compensation and the absence of feasible torque boundary constraints, most conventional TSF correction schemes adopt lag-type torque compensation, which calculates instantaneous torque merely relying on the real-time sampled current at the current moment. This lagged compensation cannot timely adjust the phase reference torque allocated by the TSF. Especially under various operating conditions, the extremely short SRM commutation duration prevents timely torque deviation correction and weakens torque ripple suppression. To tackle the above drawbacks, this work develops a novel online torque correction scheme. Different from the conventional delayed torque compensation, the proposed method constructs an instantaneous torque prediction module and introduces position-dependent variable correction factors to realize segmented interval torque correction. This fundamentally reduces commutation torque ripple and guarantees smooth torque output. The control block diagram of the proposed strategy is shown in Fig. 2.

In the sampling period T_s, Equation (1) and Equation (2) are discretized using the first-order Euler method [25], and the ex-

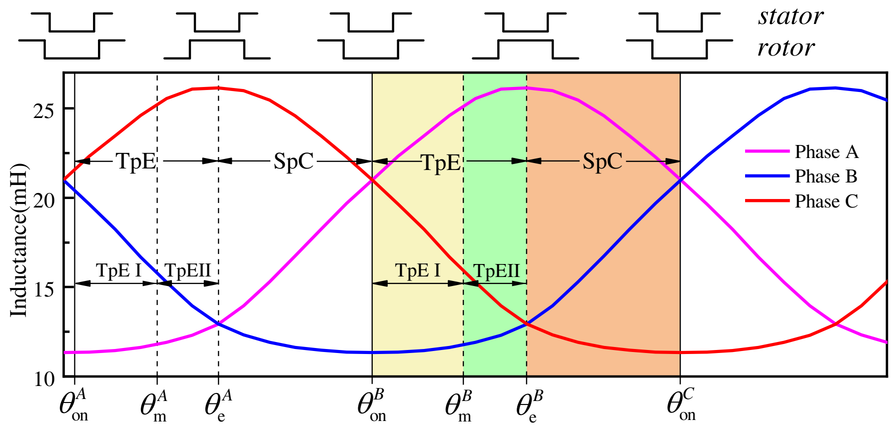

FIGURE 4. Inductance profile and division of commutation regions.

pression is written as follows:

$$\begin{cases} i_{k+1} = i_k + \frac{U_{k+1} - R_k i_k - \omega_k \cdot \frac{\partial \psi_k}{\partial \theta_k}}{\frac{\partial \psi_k}{\partial i_k}} \cdot T_s \\ \theta_{k+1} = \theta_k + \omega_k \cdot T_s \end{cases} \tag{6}$$

According to Equation (6), the phase current i_{k+1} and rotor position angle θ_{k+1} in the next control interval can be predicted from the phase voltage U_{k+1}, phase current i_k, rotor angular velocity ω_k, and flux linkage ψ_k.

In this paper, two voltage states are adopted, namely positive DC bus voltage and negative DC bus voltage, corresponding to the excitation and demagnetization operating modes of the SRM, respectively. By applying positive and negative voltage states, the upper and lower limits of the phase current in the subsequent control interval can be predicted. Based on the predicted phase current i_{k+1} and rotor position θ_{k+1}, the corresponding maximum and minimum torque values can be obtained from the $T(i, \theta)$ lookup table, thereby defining the torque range that can be achieved. This torque range provides a foundation for the online correction of the TSF strategy. The purpose of the correction process is to ensure that the adjusted torque T_{adj} remains within the predicted torque boundaries, which helps reduce the torque ripple during the commutation process.

Based on the motor's inductance characteristic curves, the single-phase conduction cycle was divided into two-phase exchange regions 1 and 2 (TPE1 and TPE2), and one single-phase conduction (SPC) region, as shown in Fig. 4 [24].

The parameter θ_m is defined as the division point between the two phase exchange zones. TPE1 zone is initiated at the turn-on angle of the magnetizing phase. TPE2 zone terminates at the fully aligned position of the stator and rotor, where the inductance of the demagnetizing phase reaches its maximum.

3.2. Principles of Online Torque Correction

Conventional torque sharing function (TSF) control allocates reference torque without considering the motor's actual torque generation capability, which readily produces reference commands exceeding the motor's maximum torque limit. A position-dependent correction factor α is proposed as an adaptive weighting coefficient for segmented adaptive matching of commutation intervals. This factor generates dedicated torque compensation for the two commutation subintervals, TPE1 and TPE2: mild correction suppresses phase current peaks in TPE1, whereas enhanced compensation offsets commutation torque drop in TPE2. Combined with the piecewise partition rule of commutation zones, it dynamically smooths the reference torque toward the motor's actual torque output limit, yielding steadier output torque with reduced fluctuations.

$$\alpha = \begin{cases} 1, & \theta_{\text{on}} \le \theta < \theta_m \\ \dfrac{(\theta_{\text{ov}} + \theta_{\text{on}}) - \theta}{(\theta_{\text{ov}} + \theta_{\text{on}}) - \theta_m}, & \theta_m \le \theta < \theta_{\text{ov}} + \theta_{\text{on}} \\ 0, & \theta_{\text{ov}} + \theta_{\text{on}} \le \theta \end{cases} \tag{7}$$

θ_{ov} is the overlap angle. The position-dependent correction factor is maximized at the start of commutation to boost the torque, gradually diminishes toward the aligned position for smoothness, and resets to zero upon completion.

Figure 6 illustrates a detailed flowchart of the proposed subregion torque online correction strategy. Taking the commutation overlap zone of phases A and C as an example, the inputs for this correction algorithm include the turn-on angle, turn-off angle, overlap angle, real-time rotor position, and total reference torque. Furthermore, the pre-allocated reference torques ($T_{\text{ref}A}$, $T_{\text{ref}C}$) derived from the exponential TSF were incorporated. By utilizing the prediction model, the maximum predicted torque of phase A and the minimum predicted torque of phase C at the next sampling instant are obtained in real time, which serves as dynamic boundary constraints for the torque correction process.

When $\theta_{\text{on}} \le \theta < \theta_m$, the motor operates in the TPE1 region. At this stage, excitation phase A is turned on and exhibits insufficient torque production capability; thus, demagnetization phase C provides the primary torque output. If the reference torque of the excitation phase exceeds its physically attainable range, that is, $T_{\text{ref}A} > T_{\max A}^{n+1}$, the reference value for phase A is corrected to its maximum achievable torque, $T_{\max A}^{n+1}$. Meanwhile, the reference torque of phase C is adjusted using a factor

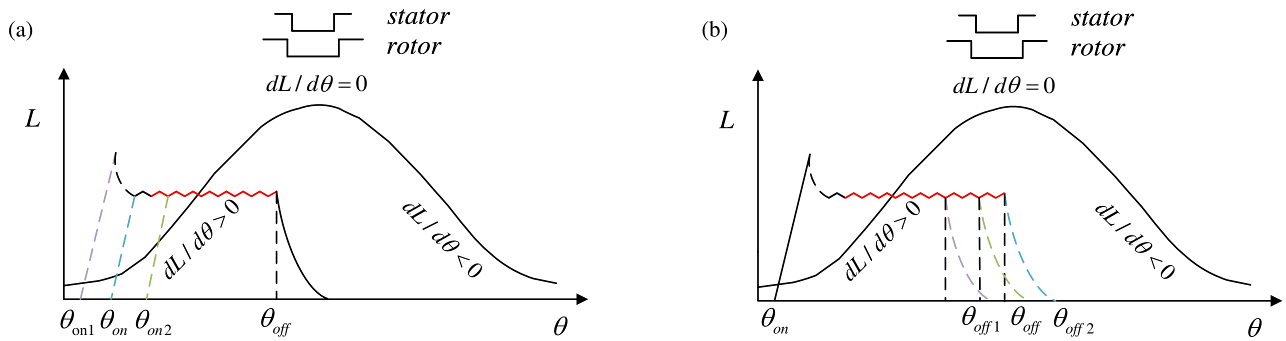

FIGURE 5. Phase current waveforms under different switching angles: (a) varying $\theta_{\rm on}$ and (b) varying $\theta_{\rm off}$.

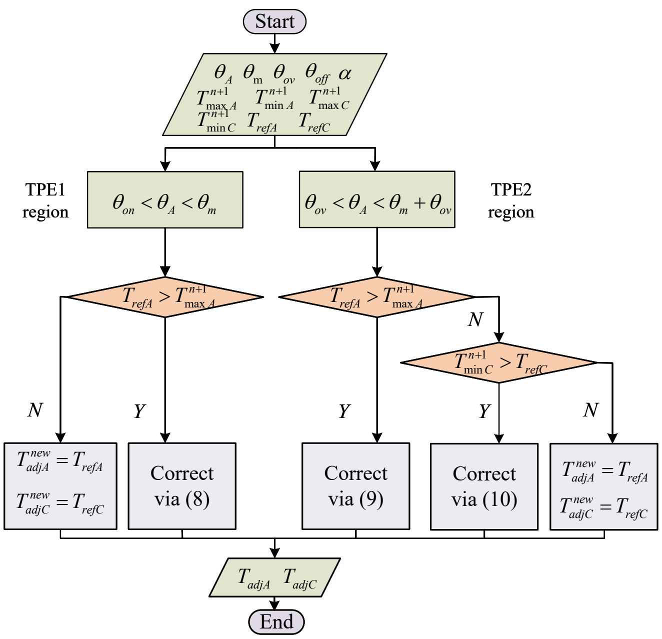

FIGURE 6. Flowchart of torque online correction control strategy.

α to compensate for the torque deficit of phase A, thereby ensuring the stability of the total output torque. The correction algorithm is formulated as in Equation (8):

$$\begin{aligned} T_{\text{adj}A}^{\text{new}} &= T_{\max A}^{n+1} \\ T_{\text{adj}C}^{\text{new}} &= T_{\text{ref}C} + \alpha(T_{\text{ref}A} - T_{\max A}^{n+1}) \end{aligned} \tag{8}$$

If $T_{\text{ref}A} < T_{\max A}^{n+1}$, the correction is not implemented, and the reference values are maintained as $T_{\text{adj}A}^{\text{new}} = T_{\text{ref}A}$ and $T_{\text{adj}C}^{\text{new}} = T_{\text{ref}C}$.

In the formula, α is the correction factor defined previously, which is used to regulate the smoothness of the torque compensation process. $T_{\max A}^{n+1}$ denotes the maximum physically attainable predicted torque for phase A at the next sampling instant, respectively.

When $\theta_m \le \theta < \theta_{\text{ov}} + \theta_{\text{on}}$, the machine operates in the TPE2 region, where the current in demagnetization phase C decreases slowly, making it prone to generating tail currents. If phase A can provide sufficient torque, the reference torque of phase C should be corrected to accelerate the current decay and suppress the tail current. Specifically, when $T_{\text{ref}C} < T_{\min C}^{n+1}$, the reference torque of phase C is adjusted to its minimum attainable torque. Meanwhile, the difference between the initial and adjusted reference torques of phase C is reallocated to phase A to compensate for the torque deficiency resulting from the correction, thereby maintaining the balance of the total output torque. The correction formulas are expressed as in Equation (9).

$$\begin{aligned} T_{\text{adj}C}^{\text{new}} &= T_{\min C}^{n+1} \\ T_{\text{adj}A}^{\text{new}} &= T_{\text{ref}A} + (T_{\text{ref}C} - T_{\min C}^{n+1}) \end{aligned} \tag{9}$$

If phase A cannot deliver the required torque, that is, $T_{\text{ref}A} > T_{\max A}^{n+1}$, its reference torque is limited to the maximum achievable predicted torque $T_{\max A}^{n+1}$ to maintain the total output torque. Simultaneously, the reference torque of demagnetization phase C is smoothly modified using the correction factor α to prevent torque fluctuations and avoid excessive current peaks. The correction is formulated as in Equation (10).

$$\begin{aligned} T_{\text{adj}A}^{\text{new}} &= T_{\max A}^{n+1} \\ T_{\text{adj}C}^{\text{new}} &= T_{\text{ref}C} + \alpha(T_{\text{ref}A} - T_{\max A}^{n+1}) \end{aligned} \tag{10}$$

If $T_{\text{ref}A} < T_{\max A}^{n+1}$ and $T_{\text{ref}C} > T_{\min C}^{n+1}$, the online correction is not executed, maintaining the reference torques as $T_{\text{adj}A}^{\text{new}} = T_{\text{ref}A}$ and $T_{\text{adj}C}^{\text{new}} = T_{\text{ref}C}$.

When $\theta_m + \theta_{\text{ov}} < \theta_a < \theta_{\text{off}}$, the motor operates within the SPC region, where the total torque is solely provided by phase A. Consequently, no torque correction is performed, preserving the profiles as $T_{\text{adj}A}^{\text{new}} = T_{\text{ref}A}$ and $T_{\text{ref}C} = 0$.

3.3. Switching Angle Optimization

Traditional TSF control strategies mostly employ fixed turn-on and turn-off angles. However, owing to the SRM's highly nonlinear nature, fixed control angles struggle to maintain optimal control performance across the entire speed and load ranges. Fig. 5 illustrates the variation of phase current with respect to the rotor position under different turn-on and turn-off angles.

As illustrated in Fig. 5(a), advancing θ_{on} boosts phase current but raises copper loss, while delayed θ_{on} results in insufficient torque. As illustrated in Fig. 5(b), an advanced θ_{off} aggravates torque ripple, whereas delayed θ_{off} produces negative torque.

Hence, dynamic adjustment of θ_{on} and θ_{off} is required to balance efficiency and torque ripple.

To evaluate the torque ripple suppression performance and copper loss characteristics of the proposed control strategy, the torque ripple coefficient T_{ripple} and root-mean-square (RMS) phase current I_{rms} are defined as follows:

$$T_{\text{ripple}} = \frac{T_{\text{max}} - T_{\text{min}}}{T_{\text{avg}}} \times 100\% \tag{11}$$

$$I_{\text{rms}} = \sqrt{\frac{1}{\theta_\tau}\left(\int_{\theta_{\text{on}}}^{\theta_{\text{off}}} i_k^2\, d\theta + \int_{\theta_{\text{on}}}^{\theta_{\text{off}}} i_{k-1}^2\, d\theta\right)} \tag{12}$$

where T_{ripple} is the torque ripple coefficient; T_{max}, T_{min}, T_{avg} denote the maximum, minimum, and average values of the output torque within a conduction period, respectively; I_{rms} represents the root-mean-square (RMS) phase current, which reflects the motor copper loss, whereas i_k and i_{k-1} are the instantaneous currents of phases k and $k-1$, respectively.

The key parameters of the PSO multi-objective optimization algorithm adopted in this paper are summarized in Table 1. The iteration terminates once the fitness fluctuation is lower than the preset threshold to reduce redundant offline calculation while guaranteeing optimization accuracy, and bilinear interpolation is used to obtain continuous optimal switching angles for arbitrary operating points.

TABLE 1. Key parameters of PSO optimization algorithm.

Parameters	Symbols (Units)	Values
Population size	N_p	50
Max iterations	G_{max}	80
Inertia weight range	w	0.8–0.5
Learning factor 1	c_1	2.0
Learning factor 2	c_2	2.0
Fitness convergence threshold	ε	10^{-4}
Speed grid resolution	Δn	200 r/min
Torque grid resolution	ΔT_L	2 N·m
Interpolation method	—	Bilinear

PSO with excellent global search performance is utilized for offline switching angle optimization across all operating points. The weighted fitness function below is established by taking the torque ripple coefficient and phase RMS current as optimization indicators:

$$\text{Fitness} = F = \omega \cdot \frac{T_{\text{ripple}}}{T_{\text{ripple,base}}} + (1-\omega) \cdot \frac{I_{\text{rms}}}{I_{\text{rms,base}}} \tag{13}$$

Both indicators are normalized by their respective reference base values to eliminate dimensional inconsistency and magnitude mismatch between the torque ripple coefficient and RMS current. In this formula, the fitness weight coefficient ω is set to 0.7. The optimal fixed inertia weight is obtained via multiple comparative optimization tests to balance the algorithm's global and local search performance.

For the fitness weight ω, comparative experiments with $\omega \in [0.5, 0.8]$ are carried out under the typical operating condition of 500 r/min and 5 N·m load. Test results confirm that ω yields minimal torque ripple and low peak current, balancing ripple reduction and copper loss, as shown in Table 2.

TABLE 2. Performance comparison under different fitness weights ω.

Fitness weight ω	Torque ripple	Phase current (A)
0.5	0.137	14.2
0.6	0.112	13.1
0.7	0.086	11.5
0.8	0.098	12.8

Further tests across all speed-load points yield identical results, verifying that $\omega = 0.7$ works well over the full operating range. The constraint conditions for this method are formulated as follows:

$$\begin{cases} -0.5 < \theta_{\text{on}} < 1.5 \\ 7.5 < \theta_{\text{off}} < 8.5 \\ T_{\text{min}} \le T_{\text{avg}} \le T_{\text{max}} \\ i_{\text{max}} < 25 \end{cases} \tag{14}$$

Note that $i_{\text{max}} < 25$ serves as the PSO peak current limit. With the prototype's 20 A rated current, this 25 A threshold reserves a 25% margin for commutation spikes to balance ripple suppression and winding thermal safety.

In this paper, switching angle optimization for the prototype machine was performed over an operating range of 0–1200 r/min in speed and 0–10 N·m in reference torque. Fig. 8 illustrates the flowchart of the proposed optimization method.

It can be observed that the optimized θ_{on} generally decreases as the motor speed and load torque increase, whereas the optimized θ_{off} exhibits an upward trend with an increase in both the motor speed and load torque. The corresponding optimization results are shown in Fig. 7.

4. SIMULATION RESULTS

To verify the feasibility and effectiveness of the proposed interval-based Torque Online Correction (TOC) control strategy, a simulation model was constructed on a MATLAB/Simulink platform using a three-phase 6/20-pole SRM as the plant. The characteristics of the phase current, torque ripple, and electromagnetic torque were thoroughly analyzed. In the simulation, the motor speed was set to 500 r/min and 1000 r/min, while the load torque was configured at 5 N·m and 8 N·m, respectively, yielding four distinct operating conditions to conduct a comparative study of three control schemes: conventional exponential TSF, the torque online correction strategy proposed in [21], and the proposed interval-based TOC method. Typical waveform comparison results are shown in Fig. 9 and Fig. 10, and the complete simulation quantitative data of the three strategies are presented in Table 3.

Figure 9 compares the torque and current performance of the three control strategies at 500 r/min and 5 N·m: the torque ripple coefficient of conventional exponential TSF is 19.2%; the

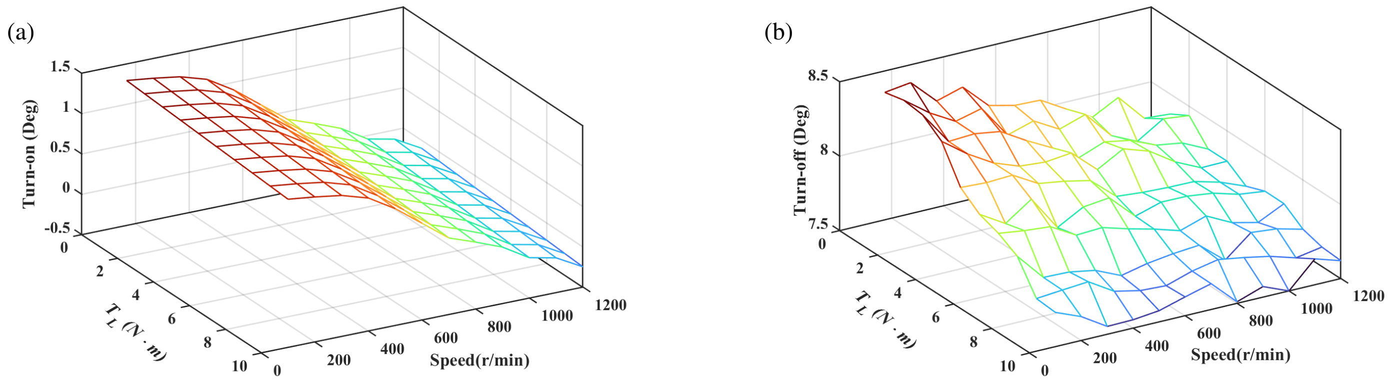

FIGURE 7. Optimization results of switching angles under different speeds and loads: (a) varying θ_{on} and (b) varying θ_{off}.

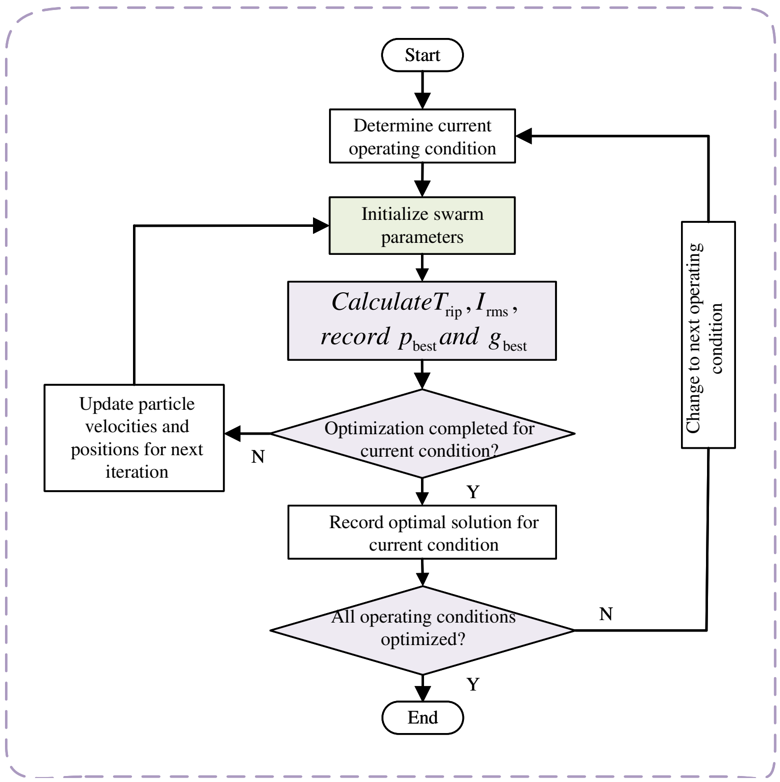

FIGURE 8. Flowchart of switching angle optimization based on the PSO algorithm.

contrast torque correction strategy in [21] reduces it to 15%, and the proposed interval-based TOC strategy further cuts it to 14%. Compared with the conventional TSF and the comparative method in [21], respectively, the proposed interval-based torque correction strategy can effectively restrain total torque ripple and peak phase current.

Fig. 12 presents the simulation waveforms of the two control strategies when the motor speed was maintained at 500 r/min and the load torque increased to 8 N·m. Compared with the traditional TSF control strategy, the output torque is in the overlap region, while the peak current decreases.

Fig. 11 illustrates the simulation comparisons between the conventional and proposed control strategies when the motor speed increases to 1000 r/min with a load torque of 5 N·m. As can be observed, under the conventional exponential TSF control strategy, the output torque fluctuates between 4.78 and 5.78 N·m; the peak phase current reaches 13.79 A; and the torque ripple coefficient increases to 20%. In contrast, with the proposed control strategy, the output torque is tightly maintained between 4.94 and 5.47 N·m; the peak phase current is suppressed to 11.5 A; and the torque ripple is restricted to 10.6%, achieving a 9.4% reduction compared with the conventional TSF method.

When the motor operates at 1000 r/min with 8 N·m load, conventional exponential TSF suffers from poor torque tracking, severe torque dips, and prominent current spikes during commutation, with a torque ripple coefficient of 32.6%. The contrast method in [21] slightly optimizes performance but

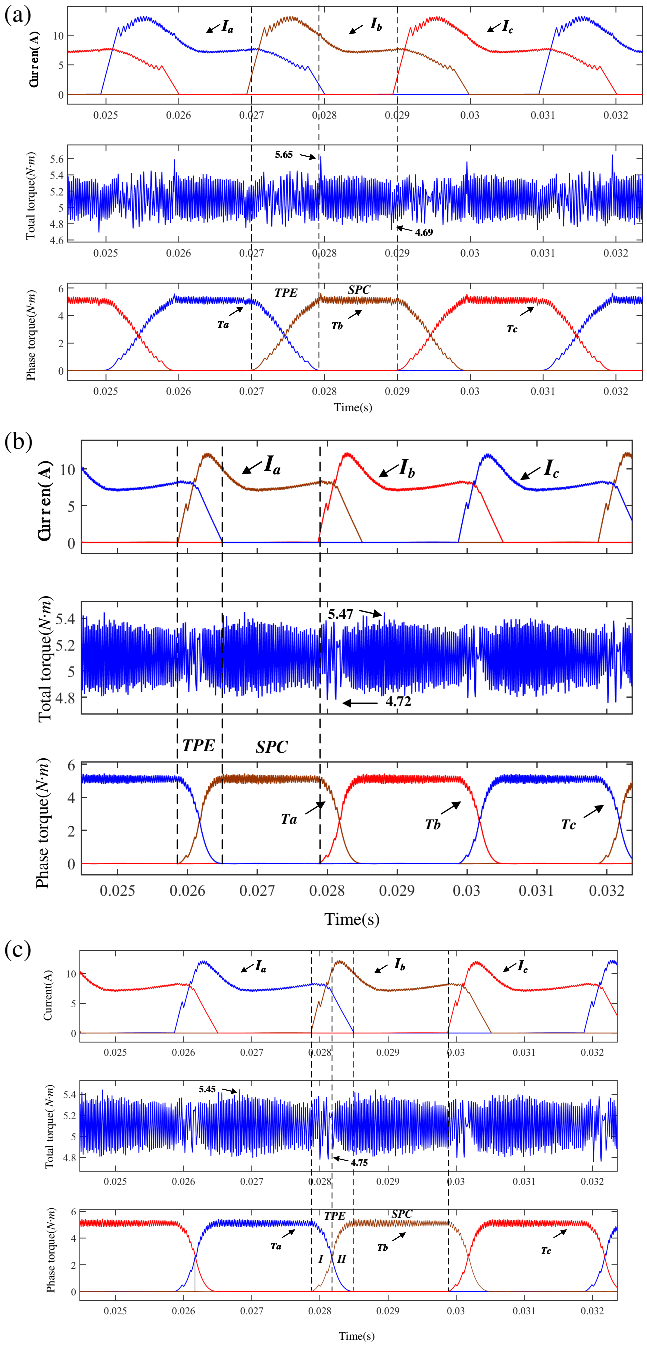

FIGURE 9. 500 r/min speed and 5 N·m load. (a) Conventional exponential type TSF, (b) TOC control strategy, and (c) proposed TOC control strategy.

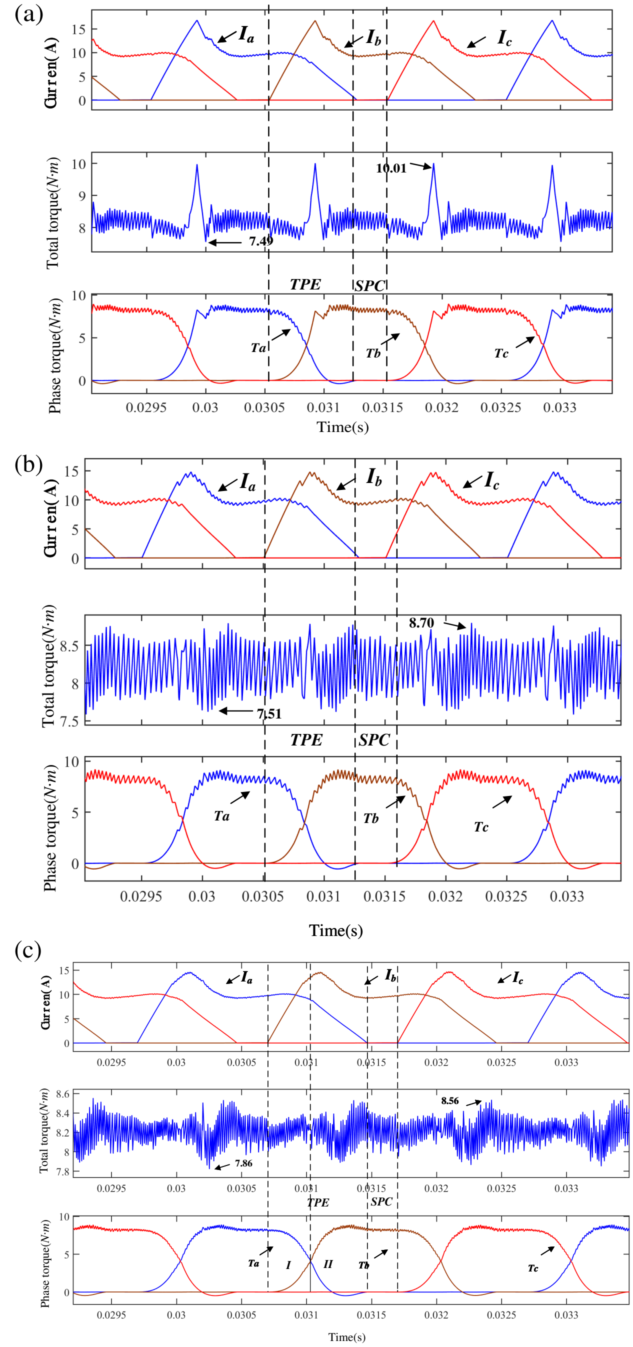

FIGURE 10. 1000 r/min speed and 8 N·m load. (a) Conventional exponential type TSF, (b) TOC control strategy, and (c) proposed TOC control strategy.

still adopts uniform compensation without commutation zoning, yielding a torque ripple coefficient of 14.88%. By contrast, the proposed interval-based TOC splits commutation into two sub-regions and applies position-variable correction under torque constraints, limiting the torque ripple coefficient to 8.75%. This zone-matched online compensation greatly alleviates torque drops and suppresses current spikes. Fig. 10 provides a full quantitative performance comparison of the three strategies under this working condition.

5. EXPERIMENT RESULTS

To further validate the effectiveness of the proposed zone-based torque online correction strategy, an experimental platform for the SRM system was established based on a prototype 6/20-pole SRM. The experimental data of the motor torque and phase currents were captured and recorded using a torque sensor and an oscilloscope. The experimental setup is illustrated in Fig. 13, and the detailed motor parameters are listed in Table 4.

Experiments were conducted using conventional and proposed control strategies under two distinct operating condi-

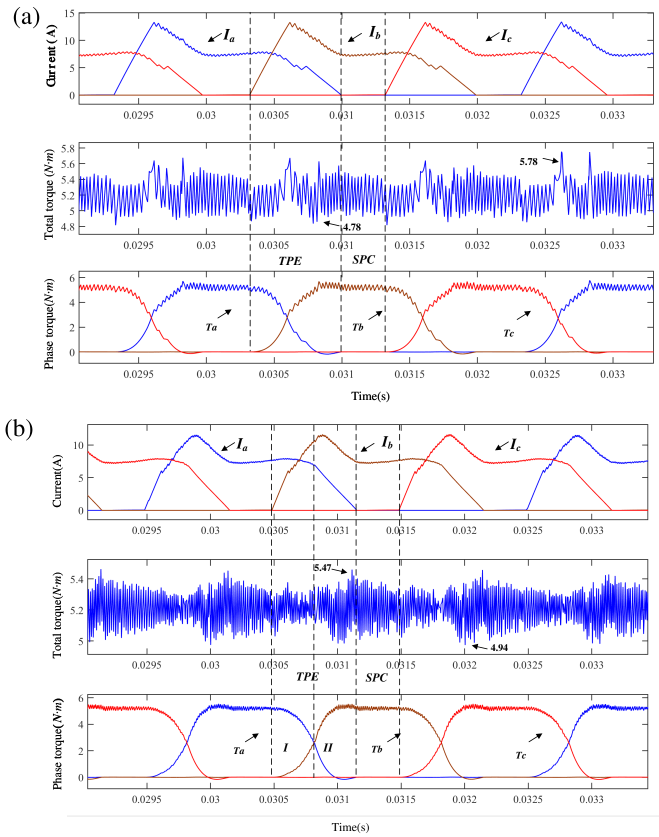

FIGURE 11. Comparison of torque and current simulation waveforms under traditional and new control strategies at 1000 r/min speed and 5 N·m load. (a) Conventional exponential type TSF and (b) proposed TOC control strategy.

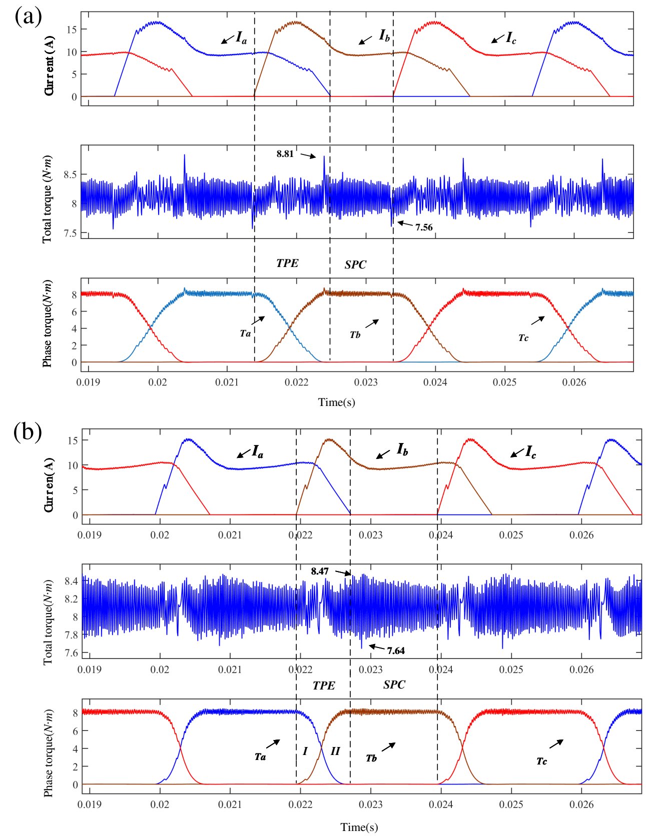

FIGURE 12. Comparison of torque and current simulation waveforms under traditional and new control strategies at 500 r/min speed and 8 N·m load. (a) Conventional exponential type TSF and (b) proposed TOC control strategy.

TABLE 3. Comparison of simulation data.

Speed (r/min)	Load (N·m)	Method	Torque Ripple (%)	Peak Current (A)
500	5	TSF	19.2	13.2
		Conventional TOC	15.0	12.8
		Partitioned TOC	14.0	12.2
	8	TSF	15.6	16.8
		Conventional TOC	12.8	16.0
		Partitioned TOC	10.4	15.4
1000	5	TSF	20.0	13.79
		Conventional TOC	14.8	12.5
		Partitioned TOC	10.6	11.5
	8	TSF	32.6	17.1
		Conventional TOC	14.88	15.2
		Partitioned TOC	8.75	14.62

TABLE 4. Parameters of the test motor.

Parameters	Symbols (Units)	Values
Number of phases	m	3
Stator/rotor poles	N_s/N_r	6/20
Stator outer diameter	D_s (mm)	143
Rotor outer diameter	D_r (mm)	172
Core length	L_c (mm)	60
Rated voltage	U_e (V)	540
Rated current	I_e (A)	20
Rated speed	n_e (r/min)	1500

tions: 500 r/min (5 N·m) and 1000 r/min (8 N·m). The comparative experimental results of the torque and current are shown in Fig. 14 and Fig. 15, respectively.

From the experimental results shown in Fig. 14, under the operating conditions of 500 r/min and 5 N·m, the peak phase current of the conventional exponential TSF strategy was 11.5 A, and the torque ripple coefficient was approximately 17.8%. In the proposed control strategy, the torque ripple coefficient was significantly reduced from 17.8% to 11.4%, accompanied by a decrease in the peak current. These experimental results successfully validate the effectiveness of the proposed control strategy.

Furthermore, as indicated by the experimental results in Fig. 15, under the conditions of 1000 r/min and 8 N·m, the conventional exponential TSF strategy exhibits a peak phase current of 15 A, a total torque fluctuation range of 6.9–9.1 N·m, and a torque ripple coefficient of 27.5%. To address the tail current issue of the demagnetization phase in the TPE2 region, the proposed control strategy implements a zone-based torque online correction method to accelerate the current decay of the

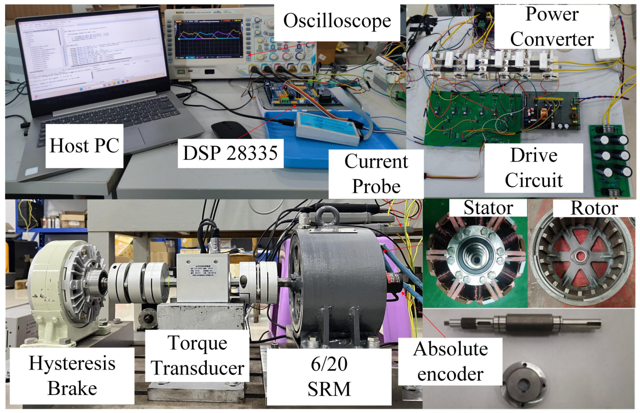

FIGURE 13. Experiment platform for testing.

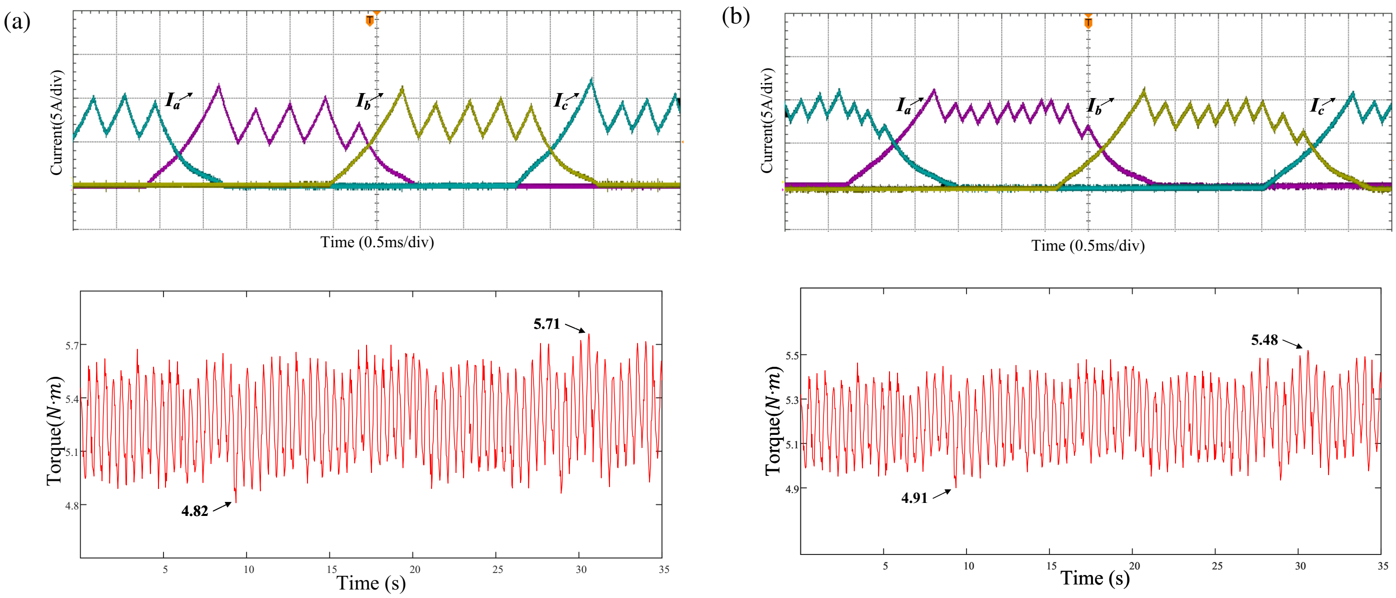

FIGURE 14. Comparison of torque and current waveforms under traditional and new control strategies at 500 r/min speed and 5 N·m load. (a) Conventional exponential type TSF and (b) proposed TOC control strategy.

outgoing phase and suppress current spikes. Consequently, the peak phase current decreased to 13.5 A; the total torque fluctuation range narrowed to 7.64–8.53 N·m; and the torque ripple coefficient was dramatically reduced to 11.3%.

In addition, owing to practical interference factors in the testing environment, including mechanical vibrations, measurement sampling noise, and DC bus voltage fluctuations, slight deviations were observed between the simulated and experimental results. Nonetheless, the consistent improvement trends remained prominent, significantly confirming the validity of the proposed control strategy.

5.1. Complexity and Real-Time Performance

To evaluate practical feasibility, the computational complexity of the proposed strategy is analyzed. The overall computational burden is naturally decoupled into two phases:

(1) Offline Optimization: Based on Equation (13), the PSO algorithm optimizes the combination of turn-on angle θ_{on} and turn-off angle θ_{off} under all operating conditions. This iterative optimization process runs completely offline on a host computer to precompute 2D lookup tables, which introduce no extra computational overhead to the real-time control loop. (2) Online Execution: The real-time control loop consists of the first-order discretized predictive model given in Equations (1)–(3), reference torque calculation with correction coefficients k_{c1} and k_{c2} shown in Equation (8) and Equation (10), as well as two-dimensional bilinear table interpolation. All these procedures only involve elementary algebraic operations including addition, subtraction, multiplication, and division, without complex transcendental functions or matrix inversion operations.

Accordingly, the total computation time T_{cal} within each sampling cycle is far shorter than the control period T_s. The proposed algorithm occupies only a small proportion of DSP core resources, leaving sufficient resource margin and fully meeting the real-time control demands of SRM drives.

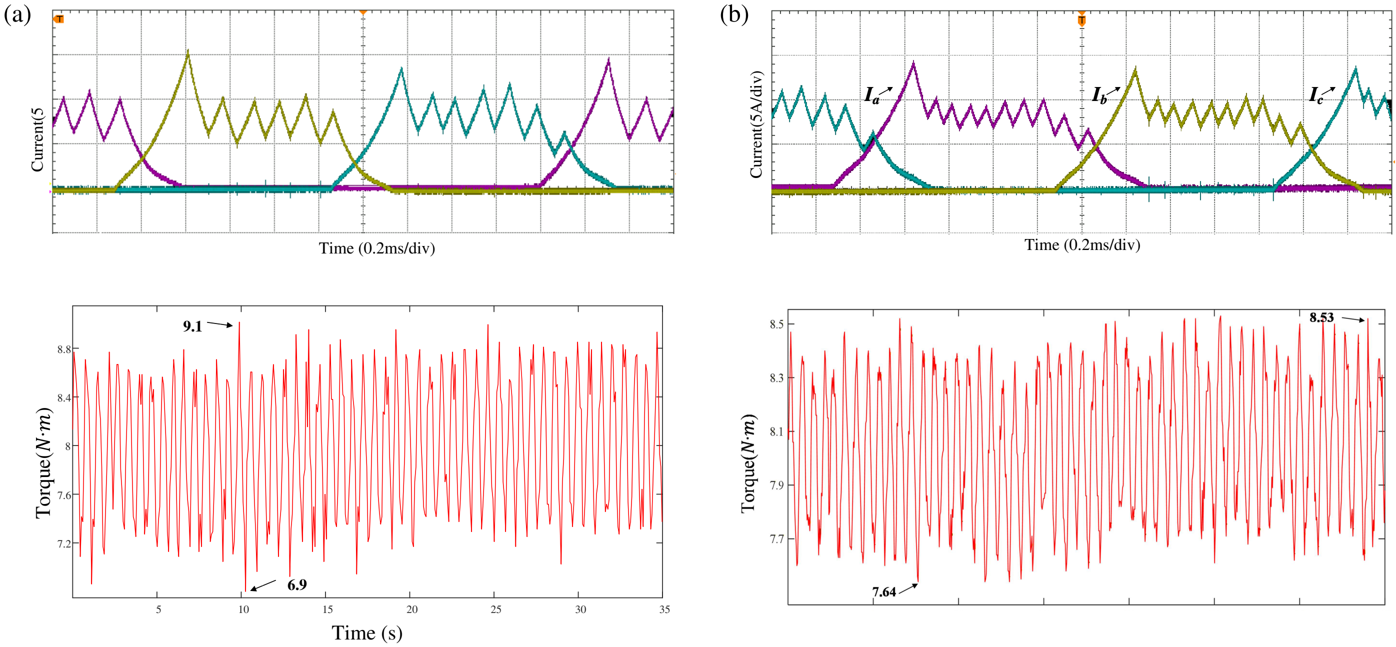

FIGURE 15. Comparison of torque and current waveforms under traditional and new control strategies at 1000 r/min speed and 8 N·m load. (a) Conventional exponential type TSF and (b) proposed TOC control strategy.

6. CONCLUSION

To address SRMs' torque ripple problem during communication intervals, this paper proposes a control strategy that combines PSO-based switching-angle optimization with zone-based online torque correction. Conventional TSF and existing torque correction methods adopt a unified compensation mechanism throughout the entire commutation cycle, without separate segmented compensation schemes designed for TPE1 and TPE2, while ignoring the motor's actual torque output limit; most of them also rely on delayed torque compensation with obvious response lag. By contrast, the proposed scheme adopts instantaneous torque prediction and position-dependent segmented correction factors, together with achievable torque boundary constraints to relieve torque mismatch and suppress current spikes and torque pulsation. Simulations and experiments under multiple working conditions compare the proposed method with conventional TSF and other mainstream correction strategies, which validate its better commutation performance and wider operating stability.

(1) Significant Reduction in Torque Ripple: Compared with the conventional TSF strategy, the proposed control method effectively mitigates the torque ripple across various operating conditions. In terms of the simulation results, the torque ripple coefficient was successfully reduced from 15.6%–32.6% under the conventional strategy to 8.75%–10.4% under the proposed method.

(2) Effective Peak Current Reduction under Identical Load Torques: While suppressing torque ripple, the proposed control strategy simultaneously reduces the peak phase current to a certain extent, thereby optimizing the comprehensive performance of the drive system.

ACKNOWLEDGMENT

This work was supported by the Natural Science Foundation of Jiangxi Province under Grant 20232BAB204063.

REFERENCES

[1] Gohari, M., A. Koochaki, and M. Divandari, "Improving switched reluctance motor drive excitation with a gaussian inductance profile in electric vehicles," *Electric Power Systems Research*, Vol. 253, 112560, 2026.

[2] Gan, C., X. Li, Z. Yu, K. Ni, S. Wang, and R. Qu, "Modular seven-leg switched reluctance motor drive with flexible winding configuration and fault-tolerant capability," *IEEE Transactions on Transportation Electrification*, Vol. 9, No. 2, 2711–2722, 2023.

[3] Liu, J., G. Wang, D. Liu, and Y. Fan, "An improved deadbeat control scheme for unipolar sinusoidal current excited switched reluctance motor drives," *IEEE Journal of Emerging and Selected Topics in Power Electronics*, Vol. 11, No. 2, 1589–1603, 2023.

[4] Fang, G., F. P. Scalcon, D. Xiao, R. P. Vieira, H. A. Gründling, and A. Emadi, "Advanced control of switched reluctance motors (SRMs): A review on current regulation, torque control and vibration suppression," *IEEE Open Journal of the Industrial Electronics Society*, Vol. 2, 280–301, 2021.

[5] Gan, C., J. Wu, Q. Sun, W. Kong, H. Li, and Y. Hu, "A review on machine topologies and control techniques for low-noise switched reluctance motors in electric vehicle applications," *IEEE Access*, Vol. 6, 31 430–31 443, 2018.

[6] Saleh, A. L., F. Al-Amyal, and L. Számel, "An enhanced current chopping control strategy for SRM drives using Harris Hawks optimization algorithm," *ISA Transactions*, Vol. 150, 338–358, 2024.

[7] De Paula, M. V., S. S. Williamson, and T. A. d. S. Barros, "Four-quadrant model following sliding mode cruise control for

SRM with DITC applied to transportation electrification," *IEEE Transactions on Transportation Electrification*, Vol. 8, No. 3, 3090–3099, 2022.

[8] Li, H., B. Bilgin, and A. Emadi, "An improved torque sharing function for torque ripple reduction in switched reluctance machines," *IEEE Transactions on Power Electronics*, Vol. 34, No. 2, 1635–1644, 2019.

[9] Al-Amyal, F. and L. Számel, "Research on novel hybrid torque sharing function for switched reluctance motors," *IEEE Access*, Vol. 10, 91 306–91 315, 2022.

[10] Song, S., G. Fang, R. Hei, J. Jiang, R. Ma, and W. Liu, "Torque ripple and efficiency online optimization of switched reluctance machine based on torque per ampere characteristics," *IEEE Transactions on Power Electronics*, Vol. 35, No. 9, 9608–9616, 2020.

[11] Wang, H. X., G. P. Wang, X. Wang, H. Chen, J. F. Pan, and L. J. Xu, "An improved torque sharing function control strategy for SRM based on a 7-level T-type converter," *Power System Protection and Control*, Vol. 53, No. 17, 57–66, 2025.

[12] Ren, P., J. W. Zhu, Y. Zhao, Y. P. Liu, Z. Jing, and S. K. Zhang, "Speed control strategy for switched reluctance motor based on dual sliding mode controller," *Proceedings of the CSEE*, Vol. 44, No. 11, 4501–4512, 2024.

[13] Yang, F., H. Chen, X. D. Li, M. P. Aguirre, and M. A. Saqib, "An efficient torque sharing function for optimizing the commutation zone control strategy of switched reluctance motors," *Transactions of China Electrotechnical Society*, Vol. 39, No. 6, 1671–1683, 2024.

[14] Ding, S., X. Huang, J. Hang, and W. Li, "Improved efficiency optimization control of srm based on redefined optimal turn-on angle and its corresponding analytical formula," *IEEE Transactions on Power Electronics*, Vol. 39, No. 12, 16 508–16 520, 2024.

[15] Kumar, M. N. and R. Chidanandappa, "Novel design and simulation of fuzzy controller for turn-on & turn-off angle in coordination with SRM speed control for electric vehicles," *Indonesian Journal of Electrical Engineering and Informatics (IJEEI)*, Vol. 10, No. 2, 246–262, 2022.

[16] Martin, G., C. A. Kumar, and J. J. Carol, "A modified crow search algorithm is used to minimize torque ripple for switched reluctance motor drives in electric vehicle application," *Journal of Intelligent & Fuzzy Systems*, Vol. 49, No. 6, 1349–1370, 2025.

[17] Ben, T., H. Wang, L. Chen, Y. Zhang, and L. Jing, "Torque ripple reduction strategy for switched reluctance motor based on segmented non-linear correction torque sharing function," *Journal of Power Electronics*, Vol. 24, No. 12, 1933–1943, 2024.

[18] Yan, W., J. Xin, K. Zhang, H. Chen, Y. Wang, X. Sun, and Q. Wang, "Torque ripple reduction of double stator switched reluctance machine with complementary inner and outer stator torques," *IEEE Transactions on Transportation Electrification*, Vol. 11, No. 4, 9602–9612, 2025.

[19] Ben, T., H. Nie, L. Chen, J. Wang, and L. Jing, "SRM torque ripple suppression strategy based on sinusoidal compensation torque sharing function," *Electric Machines and Control*, Vol. 26, No. 8, 100–111, 2022.

[20] Genc, U. and B. Tekgun, "Instantaneous torque error compensation based online torque sharing function for Switched reluctance Machines," *Alexandria Engineering Journal*, Vol. 75, 261–270, 2023.

[21] Zhang, X., Y. Mao, X. Sun, L. Feng, and Y. Xiong, "Torque online correction control of switched reluctance motor based on optimized torque sharing function," *IEEE Transactions on Energy Conversion*, Vol. 39, No. 3, 1750–1762, 2024.

[22] Sun, X., Y. Xiong, J. Yang, and X. Tian, "Torque ripple reduction for a 12/8 switched reluctance motor based on a novel sliding mode control strategy," *IEEE Transactions on Transportation Electrification*, Vol. 9, No. 1, 359–369, 2023.

[23] Song, S., S. Huang, Y. Zhao, X. Zhao, X. Duan, R. Ma, and W. Liu, "Torque ripple reduction of switched reluctance machine with torque distribution and online correction," *IEEE Transactions on Industrial Electronics*, Vol. 70, No. 9, 8842–8852, 2023.

[24] Huang, C., W. Cao, Y. Sun, Z. Chen, and W. Zhang, "A control method of switched reluctance motor based on non-unity TSF and adaptive overlapping angle," *Progress In Electromagnetics Research C*, Vol. 133, 233–249, 2023.

[25] Ge, L., J. Zhong, Q. Cheng, Z. Fan, S. Song, and R. W. D. Doncker, "Model predictive control of switched reluctance machines for suppressing torque and source current ripples under bus voltage fluctuation," *IEEE Transactions on Industrial Electronics*, Vol. 70, No. 11, 11 013–11 021, 2023.